

# COMPUTATIONAL SIMULATION OF THE FLOW PAST AN AIRFOIL FOR AN UNMANNED AERIAL VEHICLE

L. Velázquez-Araque<sup>1</sup> and J. Nožička<sup>2</sup>

<sup>1</sup> Division of Thermal fluids, Department of Mechanical Engineering, National University of Táchira, Venezuela.

<sup>2</sup> Department of Fluid Dynamics and Power Engineering, Faculty of Mechanical Engineering Czech Technical University in Prague, Czech Republic.

## ABSTRACT

This paper deals with the numerical simulation of the two-dimensional, incompressible, steady air flow past a NACA 2415 airfoil and four modifications of this one. The modification of this airfoil was made in order to create a blowing outlet with the shape of a step on the suction surface. Therefore, five different locations along the cord line for this blowing outlet were analyzed. This analysis involved the aerodynamic performance which meant obtaining lift, drag and pitching moment coefficients curves as a function of the angle of attack for the situation where the engine of the aerial vehicle is turned off called the no blowing condition by means computational fluid dynamics. The RNG k- $\epsilon$  model is utilized to describe the turbulent flow process. The simulations were held at a Reynolds number of  $10^5$ . Results allowed obtaining lift and drag forces and pitching moment coefficient and also the location of the separation and reattachment point in some cases for different angles of attack, from 0 to 16 degrees with the smallest increment of 4 degrees. Finally, numerical results were compared with results obtained from wind tunnel tests by means of an aerodynamic balance and also oil and smoke visualization techniques and found to be in very good agreement.

## INTRODUCTION

In the Laboratory of Fluid Mechanics and Thermodynamics of the CTU in Prague, an unmanned aerial vehicle (UAV) with an internal propulsion system is being developed. In order to accomplish this main objective, all the components must be designed. This paper is part of the development of an airfoil for a UAV with internal blowing propulsion system for the gliding condition.

The main motivation of this research is the validation of experimental results obtained in wind tunnel tests of the aerodynamic characteristics by means of an aerodynamic balance as well as the flow field by oil and smoke flow visualization techniques. The analysis of the air fluid flow past an airfoil from the NACA 4 digits family and four modified models is performed by means of obtaining lift and drag forces and pitching moment coefficient and also the location of the separation and reattachment point in some cases for different angles of attack. Then an exhaustive comparison to the experimental results is performed. The whole process is described in the following sections.

## AIRFOILS TESTED

A NACA 2415 airfoil (Figure 1), which has become increasingly popular on  $\frac{1}{4}$  scale pylon racers [1] was tested and also four modifications of this one. The modification is based mainly on the creation of an abrupt step on the suction side of the original NACA 2415 airfoil.

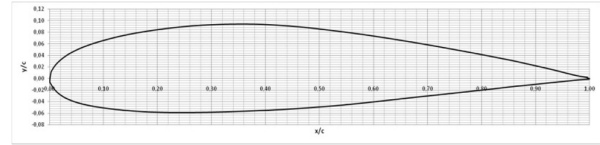


Figure 1: NACA 2415 airfoil

This step simulates a blowing propulsive outlet of the wing in normal flight conditions. Four different configurations were designed which involved the location of the step at different strategic points chordwise (Figure 2). These points are:

- At the location of the maximum thickness: 30% of the chord. (2415-3).
- At the location of the maximum camber: 40% of the chord. (2415-4).
- Before the transition point (at 0 AOA): 50% of the chord. (2415-5).
- Passed the transition point (at 0 AOA): 60% of the chord. (2415-6).

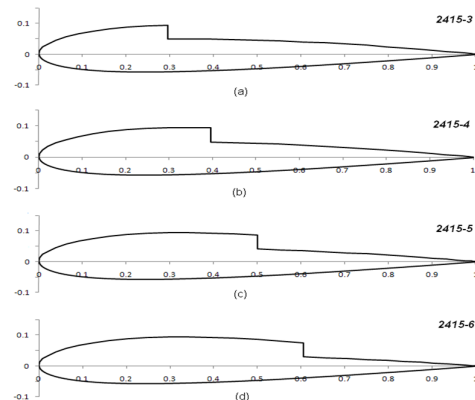
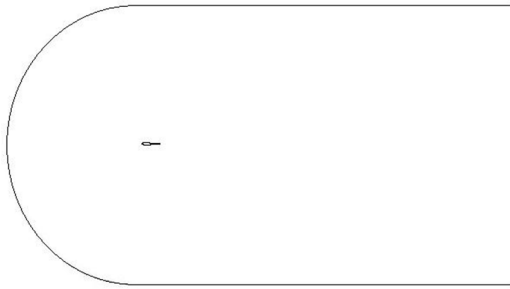


Figure 2: Airfoils developed for testing (a) 2415-3, (b) 2415-4, (c) 2415-5, (d) 2415-6.

## COMPUTATIONAL DOMAIN

Something very important in this part is the choice of the domain, because it is formed by real borders such as the upper and lower surfaces of the airfoil and also by imaginary borders which enclose the external environment. The domain extends from 8 chord lengths upstream to 20 chord lengths downstream according to [2] an also 8 chord lengths for the upper and lower heights. The fluid flow which is simulated is air past five different airfoils with a Reynolds number of  $10^5$ . These five airfoils correspond to the NACA 2415 and the four modifications with the step at 30, 40, 50 and 60 percent of the chord length. In Figure 3 it is possible to see the geometry of the domain for the airfoil 2415-3 as an example.



**Figure 3:** Computational domain for the numerical simulations

### DISCRETIZATION OF THE DOMAIN

The geometry shown in Figure 3 is discretized using a structured mesh of 188 x 200 tetrahedral elements, this mesh has been also supplemented with very small elements in the vicinity of the surface of the airfoil forming a boundary layer with a growth factor of 1,2. References when creating the mesh were followed in [3], therefore the created mesh had a size change of 2,66 and an equisize skew of 0,348.

The domain and the mesh were created using the commercial software GAMBIT, version 2.3. In order to obtain the lift and drag as a function angle of attack, single meshes were created for 0, 4, 12 and 16 degrees and for every airfoil, thus there were created a total of 20 meshes (Figure 4).

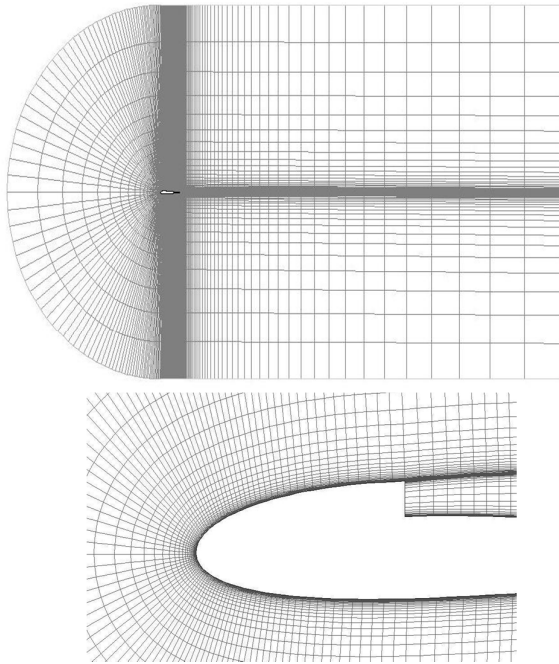


**Figure 4:** A mesh used for the numerical simulation.

Then, from the governing equations, the discretization of the domain and using the finite volume method based on finite elements, a discrete set of algebraic equations is set which solution is obtained as coupled, iteratively, using the commercial solver ANSYS FLUENT, version 12.0 using a scheme of second order upwind.

### TURBULENCE MODEL

The  $k-\epsilon$  model is derived from the Navier-Stokes equations and it is one of the simplest complete models of turbulence with two-equation models in which the solution of two separate transport equations allows the turbulent velocity and length scales to be independently determined. The standard  $k-\epsilon$  model in ANSYS FLUENT falls within this class of models and has become very used for practical engineering flow calculations. It is a semi-empirical model. It is robust, economic, and presents reasonable accuracy for a wide range of turbulent flows.

The chosen turbulence model was the RNG  $k-\epsilon$ . The RNG (renormalization group theory) is an improvement of this model of turbulence because it provides an analytically derived differential formula for effective viscosity that accounts for low-Reynolds-number effects. Therefore it is more accurate and reliable for a wider class of flows.

### BOUNDARY CONDITIONS

At the inlet it is specified the air absolute velocity magnitude and also its components; in this case the velocity is parallel to the horizontal axis, therefore it does not have any component in the ordinates. Concerning turbulence, it was also specified the turbulence intensity of 1,3 % in accordance to [4] and also the turbulent length scale. The upper and lower surfaces of the airfoil are set as walls. At the outlet it is specified the pressure as the atmospheric pressure. For the lateral walls of the domain they are set as symmetry.

### GOVERNING EQUATIONS

Since this problem does not involve heat transfer nor compressibility the equation for energy conservation is not required, therefore the most important equations such as conservation of mass and momentum used by the software's solver are listed as follows:

Continuity equation:

$$\frac{\partial \rho}{\partial t} + \nabla \cdot (\rho \vec{v}) = 0 \quad (1)$$

Conservation of momentum in a non-accelerating reference frame:

$$\frac{\partial (\rho \vec{v})}{\partial t} + \nabla \cdot (\rho \vec{v} \vec{v}) = -\nabla p + \nabla \cdot (\bar{\tau}) + \rho \vec{g} + \vec{F} \quad (2)$$

where  $p$  is the static pressure,  $\rho \vec{g}$  and  $\vec{F}$  are the gravitational and external body forces and  $\bar{\tau}$  is the stress tensor which is described as:

$$\bar{\tau} = \mu \left[ (\nabla \vec{v} + \nabla \vec{v}^T) - \frac{2}{3} \nabla \cdot \vec{v} I \right] \quad (3)$$

where  $\mu$  is the dynamic viscosity,  $I$  is the unit tensor, and the second term on the right hand side is the effect of volume dilation.

Due to the RNG  $k-\epsilon$  model was selected for the problem, the transport equations for  $k$  and  $\epsilon$  are described.

$$\frac{\partial(\rho k)}{\partial t} + \frac{\partial(\rho k u_i)}{\partial x_i} = \frac{\partial}{\partial x_j} \left( \alpha_k \mu_{eff} \frac{\partial k}{\partial x_j} \right) + G_k + G_b - \rho \epsilon - Y_M + S_k \quad (4)$$

$$\frac{\partial(\rho \epsilon)}{\partial t} + \frac{\partial(\rho \epsilon u_i)}{\partial x_i} = \frac{\partial}{\partial x_j} \left( \alpha_\epsilon \mu_{eff} \frac{\partial \epsilon}{\partial x_j} \right) + C_{1\epsilon} \frac{\epsilon}{k} (G_k + C_{3\epsilon} G_b) - C_{2\epsilon} \rho \frac{\epsilon^2}{k} - R_\epsilon + S_\epsilon \quad (5)$$

where  $k$  is the specific turbulence kinetic energy and it is defined as the variation in the velocity fluctuations; it has units  $m^2/s^2$ .  $\epsilon$  is the turbulence dissipation of small vortices (eddies), in other words, the rate at which the velocity fluctuations are dissipated, its units are  $m^2/s^3$ .

Likewise,  $G_k$  represents the generation of turbulence kinetic energy due to the mean velocity gradients.  $G_b$  is the generation of turbulence kinetic energy due to buoyancy,  $Y_M$  represents the contribution of the fluctuating dilatation in compressible turbulence to the overall dissipation rate.  $\alpha_k$  and  $\alpha_\epsilon$  are the inverse effective Prandtl numbers for  $k$  and  $\epsilon$  respectively.  $S_k$  and  $S_\epsilon$  are user-defined source terms.

### CONVERGENCE CRITERIA

The convergence criteria selected for this problem was the recommended by the software, it is  $10^{-3}$  for all the scaled residuals, however the convergence checking was deactivated because the drag and lift monitors were activated, therefore the convergence was achieved when the values of  $C_D$  and  $C_L$  remained constant for a minimum of 1000 iterations.

### RESULTS AND ANALYSIS

Figures 5 - 8 show numerical  $C_L$  versus AOA,  $C_D$  versus AOA,  $C_L$  versus  $C_D$  and  $C_M$  versus AOA for all models tested experimentally, including the original NACA 2415 airfoil.

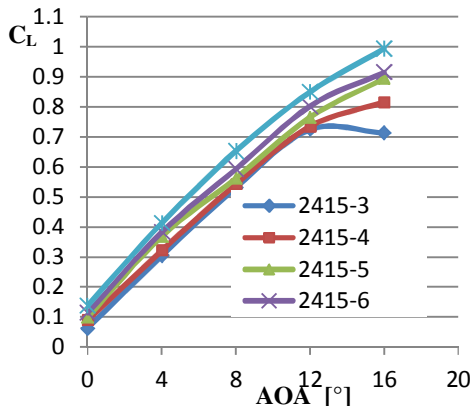


Figure 5: 2D numerical lift coefficient graph for all airfoil models tested.

In Figure 5 it is possible to see the lift coefficient as a function of AOA, the values of  $C_L$  for all AOA were obtained with CFD software. As expected the highest

lift slope corresponds to the original NACA 2415 airfoil and then, it is decreasing as the position of the step moves towards the leading edge. All slopes seem approximately straight up to 12 degrees of AOA because the minimum AOA displacement was 4 degrees. The stall point is only clear for the 2415-3 airfoil at 13 degrees of AOA; the other airfoils present a soft decreasing of the slope from 12 degrees of AOA.

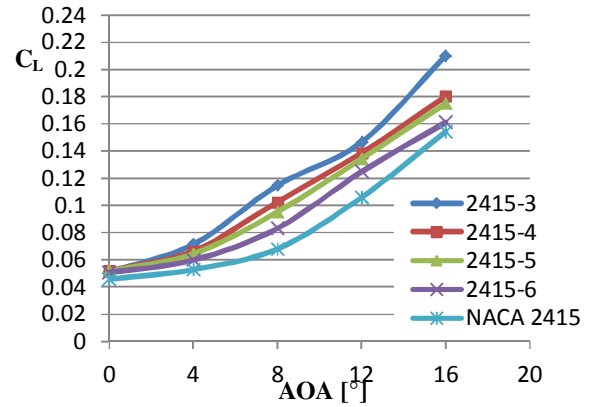


Figure 6: 2D numerical drag coefficient graph for all airfoil models tested.

In Figure 6 it is possible to see the drag coefficient as a function of AOA; the values of  $C_D$  for all AOA were obtained with CFD software. All curves begin at a common point for zero AOA approximately of 0,05  $C_D$ . After this point each curve follows its pattern and the values of  $C_D$  increase with the increment of the AOA. Among the curves, the NACA 2415 airfoil presented the lowest values of drag as expected followed by the 2415-6 and so on. This shows that the drag increases as the position of the step moves towards leading edge.

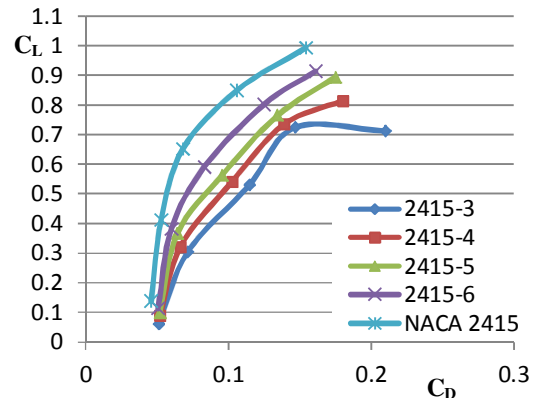


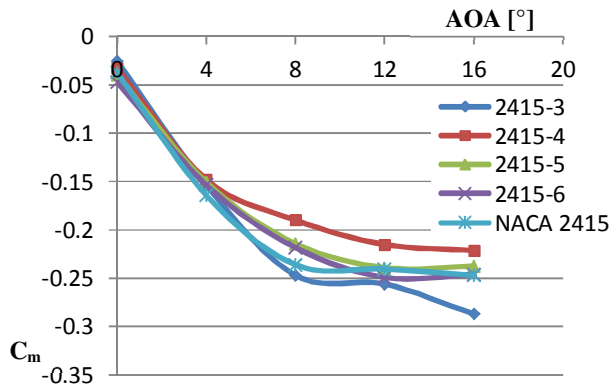
Figure 7: 2D numerical polar graph for all airfoils model tested.

Figure 7 shows the polar graph, it was also possible to obtain the Optimum Glide Ratio based on the numerical results:

- NACA 2415: OGR = 9,429.
- 2415-6: OGR = 6,944.

- 2415-5: OGR = 6,133.
- 2415-4: OGR = 5,580.
- 2415-3: OGR = 5,090.

According to this the curves it is possible to notice that the minimum drag is similar for all airfoils at 0 degrees of AOA of approximately 0,05, however, the maximum lift is obtained by the NACA 2415 of 0,993 as expected followed by the 2415-6 airfoil which presented a maximum lift of 0.914 the other maximum values of  $C_L$  can be seen in detail in Figure 7 and these ones decrease as the step moves towards the leading edge.



**Figure 8:** 2D numerical pitching moment graph for all airfoils models tested.

The numerical pitching moment coefficient was obtained with CFD software; it is computed with respect to the leading edge for several values of AOA (Figure 8). In this graph it is possible to observe that all airfoils tested presented a very similar behavior between 0 and 4 degrees of AOA, from this point the 2415-4 airfoil presents the lowest values, followed by 2415-5, 2415-6 and NACA 2415 which are very small. The 2415-3 airfoil presents the highest values of pitching moment, however this values are not so high compared to the other airfoils.

In Figure 9 it is possible to see the numerical wall shear stress on the suction surface along the chord line for the NACA 2415-3 airfoil tested from 0 to 16 degrees of AOA which allows observing points of separation and reattachment of the flow. Likewise it was possible to obtain pictures for all of the other models.

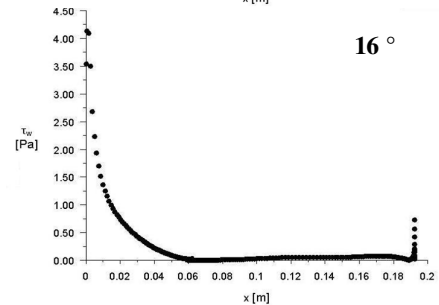
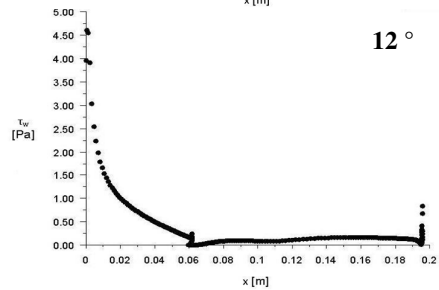
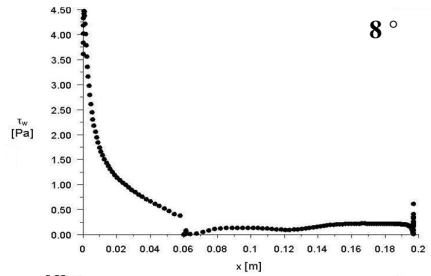
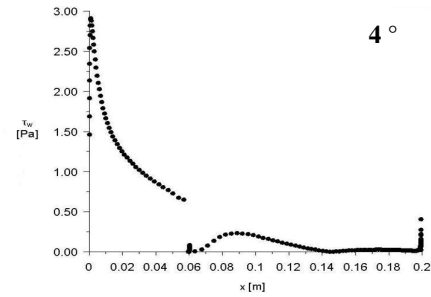
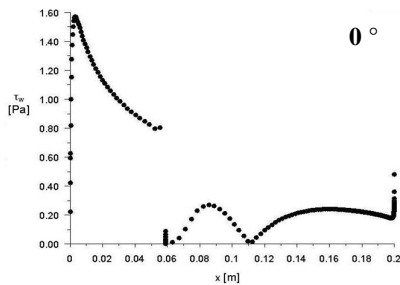


**Figure 9:** Wall shear stress of the 2415-3 airfoil for different AOA.

A shear stress is applied parallel or tangential to a face of a material. Any real fluids (liquids and gases included) moving along a solid surface will incur a shear stress on that surface. That is the reason why the wall shear stress is considered an indicative of separation of flow because when it is equal to zero, it means that the flow is not attached to the surface of the airfoil. After this point, values of shear stress are different of zero and the separation region begins. In the case of reattachment of flow, it is noticed when the values of wall shear stress reach zero again, and the area between these two points is the separation region, in this region, the values of wall shear stress are negative, this can be seen if only the x-component of the wall shear stress is plotted but for a better observation, it was decided to plot the resultant wall shear stress, where all values are always positive.

In Figure 9 it can be seen that the flow detaches at the location of the step for the 2415-3 airfoil for all AOA. It is presented as an abrupt fall in the wall shear stress curve until zero; however, for all other modified airfoils analyzed, this behavior is present until an AOA of 12 degrees; at 16 degrees of AOA the separation point is located before the step. Concerning reattachment of flow, it is observed for AOA between 0 and 4 degrees, after the step. At higher AOA there is not reattachment of flow. The NACA 2415 airfoil presented a separation point for an AOA of 4 degrees located at 95% of the chord and while the AOA was increasing, this separation point was moving towards the leading edge until reaching 30% of the chord for 16 degrees of AOA, this is important because it explains why the separation of flow for the modified airfoils begins to be present before the step for an AOA of 16 degrees.

In Figure 10, it is possible to observe the flow field as velocity contours of the air flow past the NACA 2415-6 airfoil tested from 0 to 16 degrees of AOA.

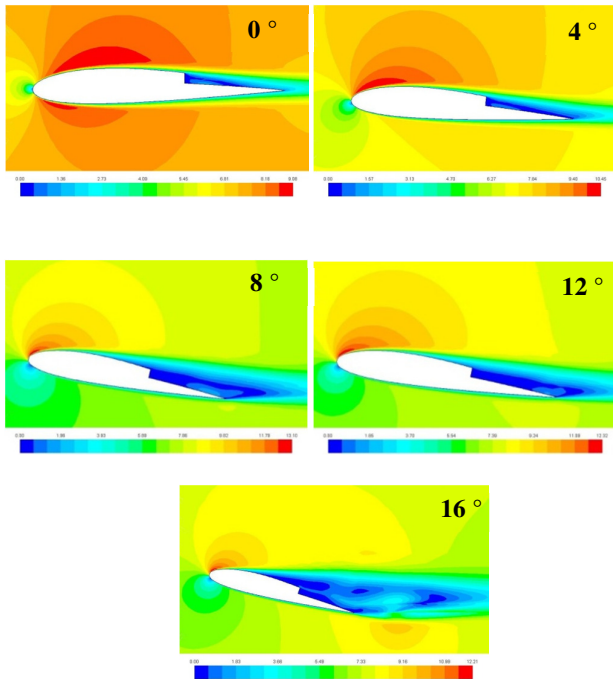


**Figure 10:** Wall shear stress of the 2415-6 airfoil for different AOA.

In Figure 10 it is possible to see the first numerical graphical approach to the behavior of the air flow past the tested airfoils. Here we can observe how the velocity changes in the selected domain; in this case the most important is to observe this phenomenon near the surface of the model. However these pictures do not show clearly the separation and reattachment points. The 2415-6 airfoil presents the biggest regions of high speed for all AOA and the reason is because the step is located closer to the leading edge so that the flow is attached to the airfoil's surface for a longer

distance than the other modified models. On the contrary, the 2415-3 airfoil presents the smallest regions of high velocity for all AOA this and therefore the biggest regions of separation of flow for all AOA this incurs a higher drag compared to other tested models.

In Figure 11 it is possible to see the streamlines of the flow past the 2415-4 airfoil.

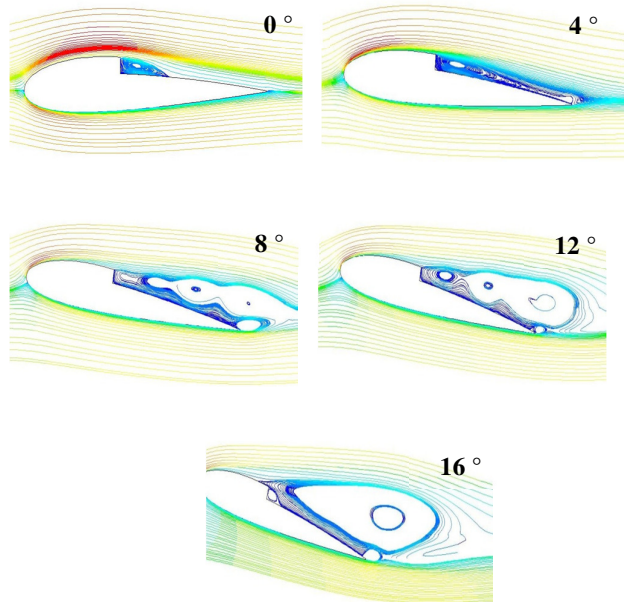


**Figure 11:** Streamlines of the 2415-4 airfoil for different AOA.

It is observed that the flow is fully attached to the suction surface of the airfoil until the step where separation of flow occurs, this phenomenon occurs for all AOA, the spatial extension of the separation region can be detected by exploring the wall shear stress along the surface of the airfoil (Figure 9). Inside this region, it is possible to observe that the adverse pressure gradient causes a reversed flow and this becomes into a counter-rotating vortex. Then the flow reattaches again and remains in contact with the surface until the trailing edge, this reattachment was observed in all modified airfoils from 0 to 4 degrees of AOA.

In Figure 11 for the 2415-4 airfoil, a very interesting phenomenon occurs at 16 degrees of AOA, a small induced vortex appears just next to the step inside the big separation region which begins upstream.

For the NACA 2415 airfoil, the streamlines remain attached along the whole surface of the airfoil until 8 degrees of AOA where a small detachment is observed very close to the trailing edge. As the AOA increases, this separation region begins more upstream. For the highest AOA, a big counter-rotating vortex is observed within the separation region.

## ANALYSIS AND DISCUSSION

This section is devoted to different comparisons between obtained experimental and numerical results.

### Comparison to force and moment coefficients obtained by wind tunnel tests.

Concerning the lift coefficient, experimental and numerical results are in good agreement; it is possible to see in Figure 12, where only two airfoils have been included on purpose for a better appreciation, that the differences are very small, for the case of the 2415-3 airfoil, the stall point could be seen clearer in the experimental results because this method had a smaller increment of the angle of attack [5].

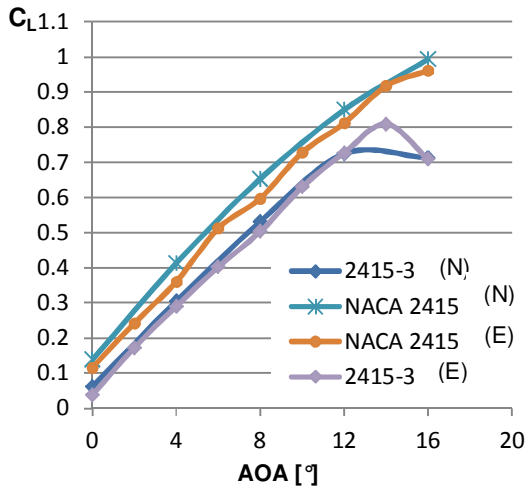


Figure 12: Numerical and experimental lift coefficient for two airfoils tested.

The behavior of the other airfoils is pretty similar and for that reason the curves were omitted.

Concerning the drag coefficient, experimental and numerical results are similar, however some discrepancies are present. In Figure 13 are shown the most representative cases of those discrepancies, only two airfoils have been included on purpose for a better appreciation. It is possible to see that in general, the numerical values for drag coefficients resulted slightly lower than the experimental ones. Since the method of computing forces used by the software consists in summing the dot product of the pressure and viscous forces on each face with the specified force vector, in this case the force is parallel to the flow direction, only abscissas, therefore, the theory of the software which predicts the force and then the coefficient does not seem very accurate.

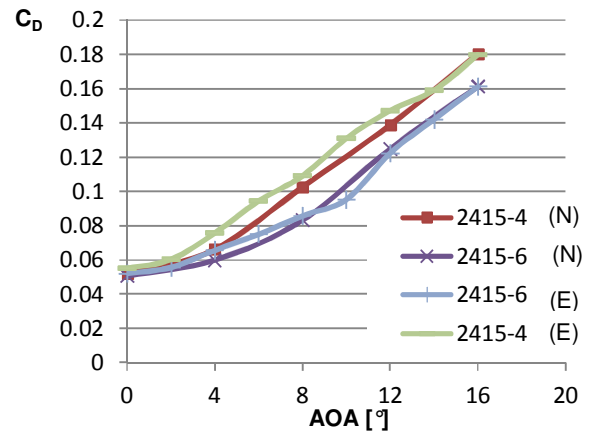


Figure 13: Numerical and experimental drag coefficient for two airfoils tested.

Concerning the pitching moment coefficient it is possible to observe in Figure 14 that experimental and numerical results present significant differences, for instance in these two cases experimental results are lower than numerical ones and so on for the rest of the models tested.

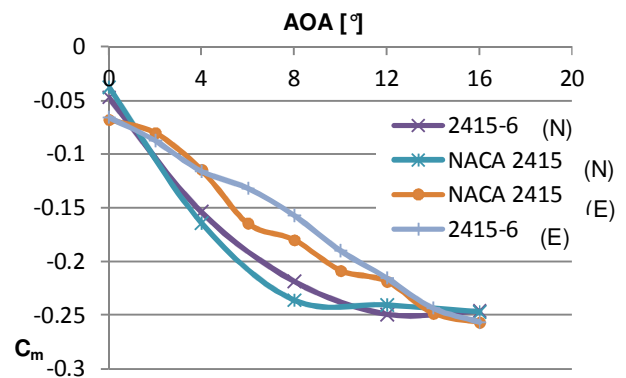


Figure 14: Numerical and experimental pitching moment coefficient for two airfoils tested.

The theory of the software which predicts the pitching moment and then its coefficient consists in summing the cross products of the pressure and viscous force vectors for each face with the moment vector, which is the vector from the specified moment center to the force origin. Based on this it can be said that these differences could be due to possible inaccuracy in the measurements with the wire balance. For a clearer determination of these discrepancies it would be necessary performing these measurements with another type of balance and compare the results [5].

### Comparison to results obtained by experimental oil and smoke visualization of flow.

According to experimental results reviewed in [6], numerical results are quite in good agreement. For instance, in Figure 15 it is possible to see a larger view of the oil visualization for the 2415-3 airfoil at 0 degrees

AOA, the values of points of separation and attachment are in very good agreement with numerical ones which are shown in Figure 16 for the same airfoil at 0 degrees of AOA.

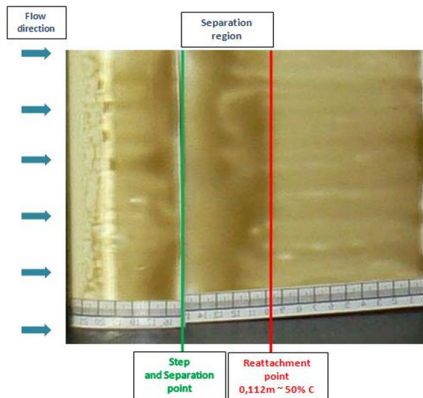


Figure 15: Oil visualization of flow for the 2415-3 airfoil at 0° of AOA.

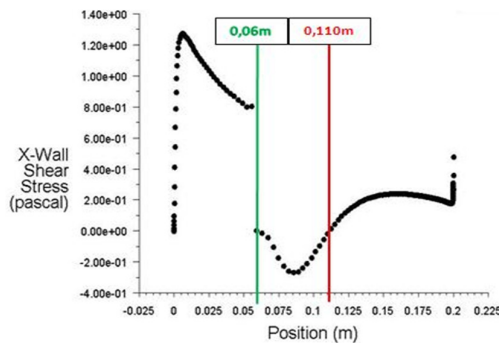


Figure 16: X-Wall shear stress for the 2415-3 airfoil at 0° of AOA.

Likewise streamlines obtained numerically were compared to smoke visualization pictures reviewed in [6]. Figures 17 and 18 are shown as an example to confirm the good agreement between numerical and experimental results.

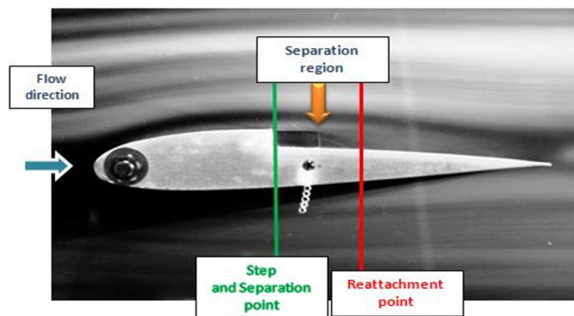


Figure 17: Smoke visualization of flow for the 2415-4 airfoil at 0° of AOA.

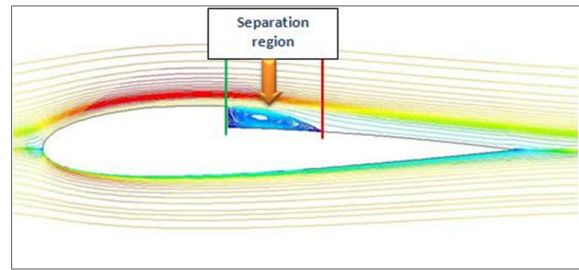


Figure 18: Streamlines for the 2415-4 airfoil at 0° of AOA.

## CONCLUSION

By means of the use of CFD it has been possible to obtain lift, drag and pitching moment coefficients and also the flow field of air past an original NACA 2415 airfoil and four modifications of this one. It was also possible to obtain the location of separation and reattachment points in some cases for different angles of attack which made possible the analysis of the influence of the location of the propulsing outlet along the chord line, turning out that for the non-blowing condition the aerodynamic performance of the airfoil increases as the propulsing outlet moves towards the trailing edge. The validation of the results has been performed through an exhaustive comparison to experimental obtained results for forces and moments by means of wind tunnel tests and separation and reattachment points by means of oil and smoke visualization having found them in good agreement.

## REFERENCES

- [1] Selig M.S., Lyon C.A., Giguere P., Ninham C., Guglielmo J.J.: *Summary of Low-Speed Airfoil Data*, Vol. 2, Virginia Beach, SoarTech Publications, 1996.
- [2] Malan P., Suluksna K., Juntasaro E.: *Calibrating the  $\gamma$ - $Re_\theta$  Transition Model for Commercial CFD*. Proceedings of The 47<sup>th</sup> AIAA Aerospace Sciences Meeting, 2009.
- [3] Rhie C.M., Chow W.L.: *Numerical Study of the Turbulent Flow Past an Airfoil with Trailing Edge Separation*, AIAA Journal, Vol. 21, No. 11, 1983.
- [4] <http://profily.fs.cvut.cz/>, Laboratory of Department of Fluid Dynamics and Power Engineering of the CTU in Prague. Section Airfoils and Straight Blade Cascades.
- [5] Velazquez L., Nožička J., Vavřín J.: *Experimental Measurement of the Aerodynamic Characteristics of Two-Dimensional Airfoils for an Unmanned Aerial Vehicle*, Proceedings of Experimental Fluid Mechanics 2010. Liberec, 2010.
- [6] Velazquez L., Nožička J., Kulhanek R.: *Oil and Smoke Flow Visualization past Two-Dimensional Airfoils for an Unmanned Aerial Vehicle*, Proceedings of The 11th Asian Symposium of Visualization. Niigata, Japan. 2011